Computers and Geotechnics 110 (2019) 57–70

Contents lists available at ScienceDirect

Computers and Geotechnics

journal homepage: www.elsevier.com/locate/compgeo

Research Paper

Multishear bounding surface modelling of anisotropic sands accounting for fabric and its evolution

Huolang Fang[a,b], Yang Shen[a], Yu Zhao[a,b,*]

[a] College of Civil Engineering and Architecture, Zhejiang University, 866 Yuhangtang Road, Hangzhou 310058, China
[b] MOE Key Laboratory of Soft Soils and Geoenvironmental Engineering, Zhejiang University, Hangzhou 310058, China

ARTICLE INFO

Keywords:
Anisotropy
Sand
Constitutive model
Fabric evolution
Dilatancy
Critical state

ABSTRACT

This paper presents a multishear bounding surface model for sands that considers evolving fabric anisotropy. The model is formulated by decomposing the overall response into a macro volumetric response and a set of spatially distributed micro shear responses. The micro stress–strain and stress–dilatancy relationships are defined for each direction of the micro shear structure. The evolving fabric tensor and anisotropic state parameter are used to characterize changes in the anisotropic structure and to satisfy the anisotropic critical state theory. The model performance is validated by the test data under different confining pressures, densities, loading modes, and loading directions.

1. Introduction

Sand deposits usually exhibit fabric anisotropy owing to gravitational sedimentation or artificial densification. The fabric anisotropy has an important influence on the sand response and needs to be carefully taken into account in the design of infrastructures related to sand deposits. Recently, the fabric anisotropy of sands and its evolution have attracted increasing attention and have become one of the main topics of experimental and theoretical studies in soil mechanics and geotechnical engineering problems.

Over the past several decades, the effects of the magnitude of fabric anisotropy and the inclination of fabric structure relative to the direction of loading on sand responses have been experimentally investigated. For instance, Yoshimine et al. [1] carried out a set of triaxial compression and extension tests, hollow cylindrical torsion shear tests, and simple shear tests on Toyoura sand under undrained loading. Their experimental results indicated that the undrained stress–strain curves and stress paths are strongly associated with the inclination of the principal stress relative to the sedimentary axis of a sand specimen. Yang et al. [2] studied the impact of anisotropic fabric on the deformation and strength of sands through undrained triaxial extension and compression tests and concluded that the undrained shear behavior in the triaxial extension is more contracting and softening than that in the triaxial compression. Sun et al. [3] investigated the failure and softening behavior of dense sands under three-dimensional stress conditions using a true triaxial apparatus. Sze and Yang [4] conducted a systematic experimental investigation into the effects of sample preparation on the cyclic loading behavior of saturated sands, including the deformation pattern, pore-water pressure generation, stress–strain relationship, and cyclic shear strength. Yang and Luo [5] investigated the relationship between the critical state and the particle shape through macro-scale and micro-scale laboratory experiments in conjunction with interpretation and analysis in the framework of critical state soil mechanics. Oboudi et al. [6] carried out triaxial compression tests under drained conditions on sand specimens prepared at two different orientations of material axes and revealed that the strain and stress behaviors of dense sands depend significantly on the direction of loading.

Although some of the experimental studies mentioned above revealed some microstructural characteristics of the sand fabric, it is not easy to quantitatively measure the evolution process of the fabric with regard to the critical state [7]. Recently, as a micromechanical numerical analysis approach, the discrete element method (DEM) has turned into an efficient means to investigate the physical and mechanical characteristics of granular materials. Some microstructural studies have focused on the fabric evolution and the uniqueness of the critical state. For example, Li and Li [8] investigated the anisotropic behavior of granular materials through two-dimensional DEM simulations, and showed that a void-based fabric tensor evolves toward the same direction and anisotropy intensity when virtual specimens with different initial fabrics deform toward the critical state. Yimsiri and Soga [9] studied the influences of an initial fabric and its evolution on

* Corresponding author at: College of Civil Engineering and Architecture, Zhejiang University, 866 Yuhangtang Road, Hangzhou 310058, China.
E-mail addresses: fanghuolang@zju.edu.cn (H. Fang), syangsdu@qq.com (Y. Shen), zhao_yu@zju.edu.cn (Y. Zhao).

https://doi.org/10.1016/j.compgeo.2019.02.015
Received 21 September 2018; Received in revised form 16 January 2019; Accepted 12 February 2019

Nomenclature

A	fabric anisotropy variable
b	intermediate principal stress ratio
d_1	dilatancy parameter
D_{ijst}	stiffness tensor
e, e_c	current and critical state void ratios
e_A, e_Γ	model parameters
e_{ij}^p	plastic deviatoric strain tensor
F_{d0}	initial fabric norm
F_{ij}, F_{ij}^d	fabric tensor and deviatoric fabric tensor
f_b, f_c, f_d, f_m	macro model surfaces
$f_b^{(nk)}$, $f_c^{(nk)}$, $f_d^{(nk)}$, $f_m^{(nk)}$	micro model lines
G_e	elastic shear modulus
$G^{(nk)}$, $G_e^{(nk)}$, $G_p^{(nk)}$	micro total, elastic, and plastic shear moduli
G_0	shear modulus parameter
$g(\theta)$	yield shape function
$h(x)$	heaviside step function
h_1, h_2, h_3	model parameters
$H^{(nk)}$, $H_p^{(nk)}$	micro total and plastic shear moduli
I_1, I_2, I_3	stress invariants
K, K_e, K_p	total, elastic, and plastic bulk moduli
K_0	initial consolidation stress ratio
k_1, k_2, k_F	model parameters
$\mathbf{I}$	unit tangential vector
M_b, M_c, M_d, M_m	bounding, critical, dilatancy, and maximum stress ratios in triaxial compression
$\mathbf{m}$	unit tangential vector
$\mathbf{n}$	unit normal vector
n_b, n_c, n_d	model parameters
$N_{ij}^{(nk)}$	projection tensor
p	mean effective stress
p_a	atmospheric pressure
p_c	initial consolidation stress
p_m	maximum mean effective stress
p_r	projection center of mean effective stress
R	stress ratio invariant
r_{ij}	stress ratio tensor
$r^{(nk)}$	micro stress ratio
$r_b^{(nk)}$, $r_c^{(nk)}$, $r_d^{(nk)}$, $r_m^{(nk)}$	micro bounding, critical, dilatancy, and maximum stress ratios
$r_r^{(nk)}$	projection center of micro stress ratio
s_{ij}	deviatoric stress tensor
t_{ij}	tensor of normalized deviatoric loading direction
$w^{(m)}$	weight coefficient
α	angle between major principal stress and vertical axis
δ_{ij}	Kronecker delta
ε_1, ε_2, ε_3	major, intermediate, and minor principal strains
ε_{ij}, ε_{ij}^p	total and plastic strain tensors
ε_q^p	equivalent deviatoric plastic strain
ε_v, ε_v^e, ε_v^p	total, elastic, and plastic volumetric strains
ε_{vd}	volumetric strain caused by dilatancy
$\varepsilon_{vd}^{(nk)}$	micro volumetric strain caused by dilatancy
$\gamma^{(nk)}$, $\gamma_e^{(nk)}$, $\gamma_p^{(nk)}$	micro total, elastic, and plastic shear strains
κ, κ_0	material parameter in bulk modulus
λ, λ_0	material parameter in bulk modulus
λ_c	critical state parameter
θ	lode angle
$\rho_1^{(nk)}$, $\bar{\rho}_1^{(nk)}$	mapping distances for micro stress ratio
ρ_2, $\bar{\rho}_2$	mapping distances for mean effective stress
σ_1, σ_2, σ_3	major, intermediate, and minor principal stresses
σ_{ij}	effective stress tensor
$\tau^{(nk)}$	micro shear stress
ψ	state variable
ζ	anisotropic state parameter
$\langle x \rangle$	Macaulay bracket

the shearing characteristic of virtual granular materials in terms of two-dimensional DEM analyses. Zhao and Guo [10] conducted three-dimensional DEM simulations and indicated that the contact normal fabric of initially isotropic specimens with different void ratios reaches the same critical state. More recently, Yang and Wu [11] performed three-dimensional undrained DEM simulations and concluded that the contact normal fabric tensor at the critical state has nothing to do with the intensity of the initial fabric anisotropy. Wang et al. [12] studied the evolution characteristics of contact normal-, particle orientation-, and void vector-based fabric tensors under biaxial loading with a constant mean effective stress using the two-dimensional DEM. The results confirmed the existence of a unique fabric tensor at the critical state for these three types of fabric tensors, regardless of initial void and fabric anisotropy.

On the other hand, many theoretical studies have been conducted to develop constitutive models for sands containing some initial anisotropic information of the fabric but ignoring its evolution during plastic deformation [13–24]. For example, Li and Dafalias [13] and Dafalias et al. [15] proposed bounding surface models using different anisotropic state variables associated with the inherent fabric tensor of sands. Rahimi et al. [21] presented a bounding surface model accounting for the influences of inherent fabric anisotropy for un-cemented and cemented sands and showed that the simulation values agreed well with the torsional shear test data. However, the hypothesis of a constant fabric with inherent initial fabric anisotropy during plastic deformation may sometimes lead to inconsistencies between the experimental data and model simulations. For this reason, some attempts have been made to consider the variation of fabric anisotropy during plastic deformation in constitutive models. Wan and Guo [25] and Wan et al. [26] proposed a micromechanical approach incorporating an evolving second-order fabric tensor into the stress–dilatancy relation. Li and Dafalias [27] established the theory of an anisotropic critical state. They proposed the approach by introducing an additional term with a scalar variable of fabric anisotropy, which is defined as the double dot product of the tensor of the normalized deviatoric loading direction and the tensor of the deviatoric fabric into the expression of Been and Jefferies's state parameter [28]. Iai et al. [29] studied the evolution of fabric anisotropy for granular materials using the strain space multi-mechanism model. A comparison of simulation results by the model and DEM indicated that the model captured the basic characteristics of the induced fabric evolution. Kruyt [30] and Kruyt and Rothenburg [31] proposed a fabric-based micromechanical dilatancy relation and confirmed that its predicted value was in good agreement with the result of a two-dimensional DEM simulation. Recently, Gao et al. [32], Zhao and Gao [33], Woo and Salgado [34], Gao and Zhao [35,36], and Yang et al. [37] developed constitutive models with the evolution of fabric anisotropy using the approach proposed by Li and Dafalias [27]. Dashti et al. [38] presented a multilaminate model containing an evolving fabric dilatancy tensor and investigated the effect of stress-induced anisotropy on the response of liquefied sandy soils using the proposed model. In addition to the above constitutive studies of anisotropic sands, some constitutive models of anisotropic soft clays have been proposed. For example, Wheeler et al. [39] presented the S-CLAY1 model, which accounted for the initial anisotropy of soft clays and its evolution. Castro and Karstunen [40] studied the installation effects of stone columns in natural soft clays using the S-CLAY1 model. Rezania et al. [41,42] investigated the performance of the S-CLAY1 model by changing the yield function equation and predicted the behavior of natural soft clay

deposits during the installation of a pile with this model.

This study proposes a multishear bounding surface model for sands considering the influence of fabric anisotropy and its evolution. A constitutive formulation is obtained based on the multishear concept that the macro constitutive response can be split into a macro volumetric response and a set of spatially distributed micro shear responses associated with virtual micro shear structures [43,44]. This concept originated from the slip theory of plasticity proposed by Taylor [45] for polycrystalline metals, which was also used in the multilaminate model [17,23], the microplane model [46], and the micro-contact model [16]. Each micro shear structure characterizes three individual micro shear responses and three individual micro volumetric responses caused by dilatancy in three mutually perpendicular directions. Two micro relationships of stress–strain and stress–dilatancy are defined for each direction of the micro shear structure. The evolving fabric tensor dependent on the deviatoric plastic strain is used and the state parameter associated with a scalar variable of fabric anisotropy is introduced into the expressions for the plastic modulus and dilatancy. The applicability of the proposed model is confirmed by comparing the predicted values with the experimental data.

2. Model formulation

2.1. Framework of multishear model

The multishear framework can be considered to be a semi-multiscale modelling approach. Its basic concept is to characterize the macro constitutive relation of sands in terms of a macro volumetric response and a set of spatially distributed virtual micro shear responses associated with various micro-contacts of all possible orientations in sands. The micro-contact is randomly distributed and is a virtual representation of the contact between particles. Fig. 1 shows the representative elementary volume of sands with a unit sphere, indicating the conceptual framework for the multishear model. The normal direction of a micro-contact in yellow is defined as the unit normal vector **n** on the sphere. Corresponding to each micro-contact, a micro shear structure is defined and its direction is assumed to be the same as that of the micro-contact. The component of **n** is represented by n_i, where the subscript i (=1, 2, and 3) refers to the global Cartesian coordinate x_i. The orthogonal unit vectors **l** and **m** within the micro-contact are defined as two tangential directions of a micro shear structure. Their components are represented by l_i and m_i. The projection of a macro deviatoric strain tensor onto the micro-contact usually produces three micro strain components, one of which is normal while the other two are tangential. As the projection of a deviatoric strain tensor, they are not distinguishable apart from their different orientations. Therefore, they can be termed as the micro shear strain, given by

$$\gamma^{(nk)} = N_{ij}^{(nk)}\varepsilon_{ij}\ (k = 1,\ 2,\ 3) \tag{1}$$

where the superscript (nk) of a function refers to its kth component in the nth micro shear structure; k = 1, 2, and 3 denote the **l**, **m**, and **n** directions of a micro shear structure, respectively; $\gamma^{(nk)}$ represents the kth micro shear strain component in the nth micro shear structure; ε_{ij} denotes the macro strain tensor; and $N_{ij}^{(nk)}$ refers to the projection tensor of the kth micro shear strain component in the nth micro shear structure, expressed as

$$N_{ij}^{(n1)} = \frac{1}{2}(l_i n_j + l_j n_i),\ N_{ij}^{(n2)} = \frac{1}{2}(m_i n_j + m_j n_i),\ N_{ij}^{(n3)} = n_i n_j - \frac{1}{3}\delta_{ij} \tag{2}$$

where δ_{ij} refers to the Kronecker delta.

The corresponding kth micro shear stress component in the nth micro shear structure is defined as $\tau^{(nk)}$. By assuming that the micro shear structures are independent of each other and that the strain and stress in each micro shear structure are uniform, and by using the virtual work theorem for all strain and stress components, the macro effective stress increment can be expressed as [44]

$$\mathrm{d}\sigma_{ij} = \mathrm{d}p\delta_{ij} + \sum_{n=1}^{N}\sum_{k=1}^{3} 2w^{(n)}N_{ij}^{(nk)}\mathrm{d}\tau^{(nk)} \tag{3}$$

where σ_{ij} and $p = \sigma_{ii}/3$ refer to the tensor of the macro effective stress and the macro mean effective stress, respectively; $w^{(n)}$ represents the weight coefficient for the nth micro shear structure; and N denotes the total number of micro shear structures, which is set to 21 for an acceptable accuracy. The second term on the right side of Eq. (3) indicates that the total deviatoric stress is equal to the superposition of the micro shear stresses for all micro shear structures. Note that although the micro shear structures are assumed to be independent of each other, they are coupled macroscopically because of their integrated interactions.

2.2. Fabric tensor and its evolution

The fabric of granular materials is dependent on the shape and spatial arrangement of particles, as well as the related void and their interactions. There are several approaches to describe the intensity of the fabric anisotropy and the orientation of the particle arrangement. Most of them are associated with the particle direction, void, and contact normal. They are usually expressed by a second-order symmetric tensor F_{ij} [47]. Generally, F_{ij} can be decomposed into its spherical and deviatoric parts as

$$F_{ij} = \frac{1}{3}F_{kk}\delta_{ij} + F_{ij}^{\mathrm{d}} \tag{4}$$

where F_{ij}^{d} represents the tensor of the deviatoric fabric related to anisotropy, which is symmetric and traceless. In order to describe the magnitude of fabric anisotropy, the fabric norm is defined as $F_{\mathrm{d}} = \sqrt{F_{ij}^{\mathrm{d}}F_{ij}^{\mathrm{d}}}$. For the sake of convenience, the tensor of the deviatoric fabric is normalized so that the critical value of a fabric norm is equal to 1. For initially orthotropic sand deposits in which the x_1 - x_2 plane is located in the isotropic plane (usually sedimentary plane) and the x_3-axis is along the orientation of sedimentation, F_{ij}^{d} can be expressed as

$$F_{ij}^{\mathrm{d}} = \sqrt{\frac{2}{3}}\begin{pmatrix} -F_{\mathrm{d0}}/2 & 0 & 0 \\ 0 & -F_{\mathrm{d0}}/2 & 0 \\ 0 & 0 & F_{\mathrm{d0}} \end{pmatrix} \tag{5}$$

where F_{d0} is the initial fabric norm. Note that Eq. (5) follows the coordinate system being consistent with the sedimentary orientation of the sand deposits. If the coordinate system is not consistent with the sedimentary orientation of the sand deposits, a coordinate transformation needs to be carried out.

The existing knowledge of the fabric evolution of sands is mainly based on micromechanical investigations in terms of DEM simulations

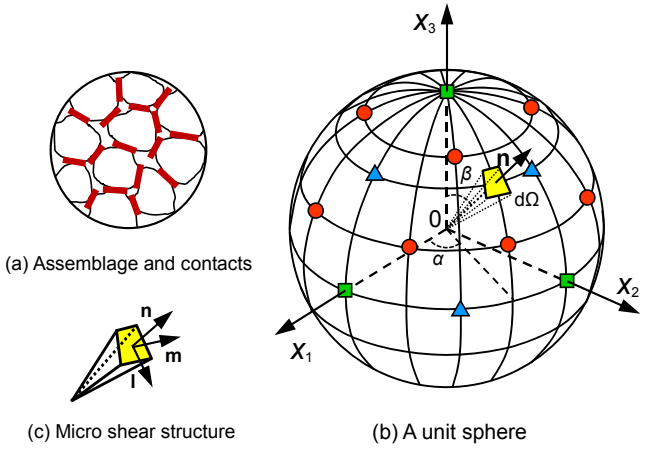

Fig. 1. Illustration of conceptal framework for multishear model.

(e.g. [8,12]). The results of the micromechanical studies indicated that the fabric structure at the critical state is associated with the loading path but has nothing to do with the anisotropy of the initial fabric. According to the study by Li and Dafalias [27], a simple fabric evolution law is adopted as

$$dF_{ij}^{d} = k_F(t_{ij} - F_{ij}^{d})d\varepsilon_q^p \tag{6}$$

where $\varepsilon_q^p = \sqrt{2e_{ij}^p e_{ij}^p/3}$ represents the equivalent macro deviatoric plastic strain; $e_{ij}^p = \varepsilon_{ij}^p - \varepsilon_{ij}^p \delta_{ij}$ refers to the tensor of the macro deviatoric plastic strain; ε_{ij}^p denotes the tensor of the macro plastic strain; and t_{ij} represents the tensor of the normalized deviatoric loading direction, which is defined as the direction of the deviatoric plastic strain increment. For triaxial monotonic loading, t_{ij} can be expressed by the deviatoric stress direction $t_{ij} = s_{ij}/\sqrt{s_{ij}s_{ij}}$, in which $s_{ij} = \sigma_{ij} - p\delta_{ij}$ denotes the tensor of the macro deviatoric stress. k_F refers to the dimensionless parameter that represents the rate of fabric evolution, given by $k_F = k_1 \exp(k_2 e)$, where e is the current void ratio, and k_1 and k_2 are model constants. The introduction of e into the expression of k_F better simulates the constitutive response of sands with different densities. Following the evolution law of Eq. (6), the sand fabric evolves toward the direction of loading along with the development of deviatoric plastic strain, and finally arrives at its critical structure.

2.3. Anisotropic state parameter

The experimental and micromechanical numerical studies showed that the void, stress level, and fabric structure significantly affect the sand response during loading. To consider the influence of the stress and void, Been and Jefferies [28] proposed a simple and effective method using a state parameter ψ, which measures the interval between the current and critical void ratios under the identical mean effective stress, defined as $\psi = e - e_c$, where e_c represents the critical void ratio. This state parameter is essentially an isotropic measure compatible with the conventional critical state theory of granular soils. Because the expression of this state parameter has nothing to do with the fabric anisotropy, it is not suitable for anisotropic sands in principle. To make this state parameter applicable to anisotropic sands, Li and Dafalias [27] proposed an approach by introducing an additional term with the scalar variable of fabric anisotropy into the expression of Been and Jefferies. This scalar variable is defined as the double dot product of the tensor of the normalized deviatoric loading direction and the tensor of the deviatoric fabric, given by

$$A = F_{ij}^{d} t_{ij} \tag{7}$$

where A represents the scalar variable of fabric anisotropy, which reaches 1 at the critical state. Following the proposition by Li and Dafalias [27], the modified state parameter is defined in a simple form as

$$\zeta = \psi - e_A(A - 1) \tag{8}$$

where e_A denotes the model constant and ζ is called the anisotropic state parameter. Note that Eq. (8) becomes identical to the expression of Been and Jefferies when the scalar variable of fabric anisotropy is equal to its critical value, which means that Eq. (8) has nothing to do with the fabric anisotropy at the critical state and satisfies the uniqueness of the critical state for anisotropic sands. The empirical expression for the critical void ratio can be written as [13]

$$e_c = e_\Gamma - \lambda_c (p/p_a)^{n_c} \tag{9}$$

where e_Γ, λ_c, and n_c represent material constants associated with the critical state; and p_a denotes the atmospheric pressure.

2.4. Macro bounding surfaces and micro bounding lines

Based on the double-hardening bounding surface theory, two kinds of macro model surfaces are defined as a cone and flat cap in shape. The conical surfaces are related to the elastoplastic loading caused by a variation in the macro stress ratio, and the cap is related to the elastoplastic loading caused by a variation in the mean effective stress under a constant stress ratio. Fig. 2 shows four conical surfaces with vertices at the origin in the principal stress space. These surfaces are determined by the macro stress ratio invariant, their stress ratios under triaxial compression, and the shape function of the yield surface as

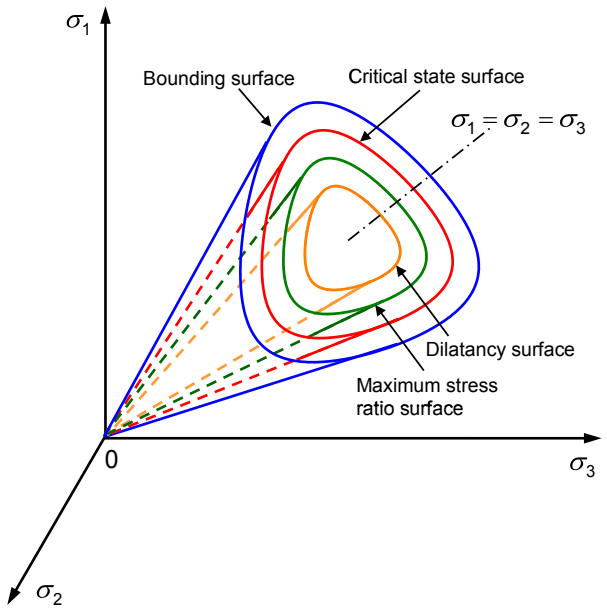

Fig. 2. Model surfaces in macro stress space.

$$f_i = R - M_i g(\theta) = 0 \quad (i = \text{b, c, d,m}) \tag{10}$$

where f_b, f_c, f_d, and f_m represent the macro bounding, critical state, dilatancy, and maximum stress ratio surfaces, respectively; $R = \sqrt{3/2 r_{ij} r_{ij}}$ denotes the macro stress ratio invariant, in which $r_{ij} = s_{ij}/p$ is the macro stress ratio tensor; $g(\theta)$ refers to the shape function of the yield surface; θ represents the Lode angle; and M_b, M_c, M_d, and M_m denote the macro bounding, critical, dilatancy, and maximum stress ratios in triaxial compression, respectively. M_m is calculated by Eq. (10) when the maximum stress ratio occurs. M_b and M_d [27] are defined as $M_b = M_c \exp(-n_b \zeta)$ and $M_d = M_c \exp(n_d \zeta)$, respectively, where n_b and n_d represent model constants.

To consider the impact of the intermediate principal stress on the yield criterion, the Matsuoka–Nakai yield criterion [48] or the Lade–-Duncan yield criterion [49] can be employed. For the Matsuoka–Nakai yield criterion, $g(\theta)$ can be expressed as

$$g(\theta) = \frac{1}{6} R\left(3\sqrt{(I_1 I_2 - I_3)/(I_1 I_2 - 9I_3)} - 1\right) \tag{11}$$

where $I_1 = \sigma_{ij}$, $I_2 = (\sigma_{ii}^2 - \sigma_{rs}\sigma_{sr})/2$, and $I_3 = \sigma_{ij}\sigma_{jk}\sigma_{ki}/3 - \sigma_{rs}\sigma_{sr}\sigma_{mm}/2 + \sigma_{nn}^3/6$ represent three stress invariants. For the Lade–Duncan yield criterion, $g(\theta)$ can be expressed as

$$g(\theta) = \frac{R}{3p}\left\{1 - \frac{1}{2}\sqrt{I_3/p^3}\left[\cos\left(\frac{1}{3}\cos^{-1}\left(-\sqrt{I_3/p^3}\right)\right)\right]^{-1}\right\}^{-1} \tag{12}$$

The bounding surface of flat cap f_p can be defined as

$$f_p = p - p_m = 0 \tag{13}$$

where p_m represents the maximum mean effective stress in the past loading process.

Corresponding to the above macro model surfaces, four micro model lines for the kth component in the nth micro shear structure, as shown in Fig. 3, are defined in the $\tau^{(nk)} - p$ plane as

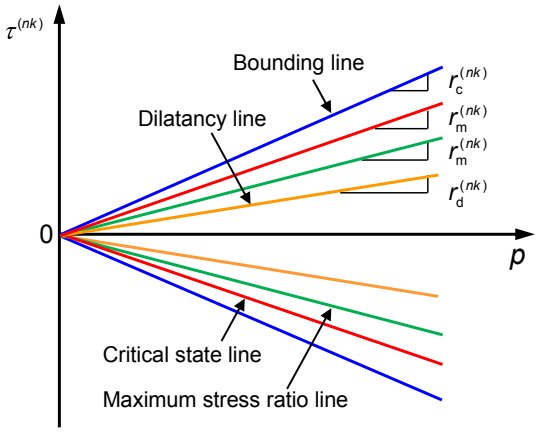

Fig. 3. Model lines in $\tau^{(nk)} - p$ plane.

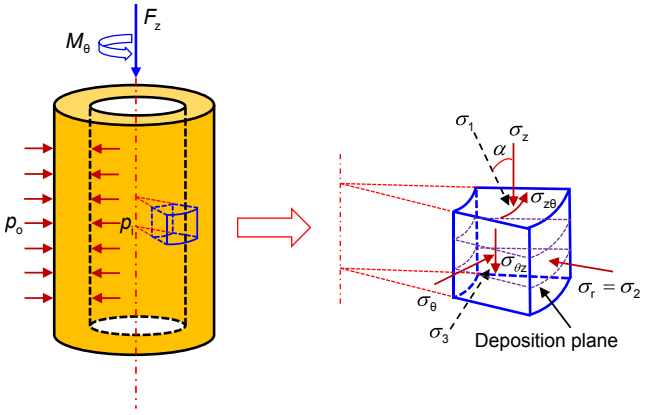

Fig. 4. Setup of a hollow cylindrical torsion shear test.

$$f_i^{(nk)} = \tau^{(nk)} - r_i^{(nk)} p = 0 \ (i = \mathrm{b},\ \mathrm{c},\ \mathrm{d}, \mathrm{m}) \tag{14}$$

where $f_b^{(nk)}$, $f_c^{(nk)}$, $f_d^{(nk)}$, and $f_m^{(nk)}$ represent the micro bounding, critical state, dilatancy, and maximum stress ratio lines for the kth component in the nth micro shear structure, respectively; $r^{(nk)} = \tau^{(nk)}/p$ refers to the micro stress ratio; and $r_b^{(nk)}$, $r_c^{(nk)}$, $r_d^{(nk)}$, and $r_m^{(nk)}$ denote the micro bounding, critical, dilatancy, and maximum stress ratios, respectively. $r_b^{(nk)}$, $r_c^{(nk)}$, and $r_d^{(nk)}$ can be calculated by the corresponding macro parameters and the yield shape function (see A.4 in the Appendix A). $r_m^{(nk)}$ is calculated by Eq. (14) when the maximum micro stress ratio occurs.

2.5. Macro volumetric deformation

The incremental stress–strain relationship for the macro volumetric deformation can be written as (see A.1 in the Appendix A for the derivation procedures)

$$\mathrm{d}\varepsilon_v - \mathrm{d}\varepsilon_{vd} = \frac{1}{K_e}\mathrm{d}p + \frac{1}{K_p}\mathrm{h}(p - p_m)\frac{\langle \mathrm{d}p\rangle}{|\mathrm{d}p|}\mathrm{d}p \tag{15}$$

where ε_v represents the macro volumetric strain; ε_{vd} denotes the macro volumetric strain caused by dilatancy; K_e refers to the elastic bulk modulus; K_p represents the plastic bulk modulus; $\mathrm{h}(x)$ denotes the Heaviside step function, given that $\mathrm{h}(x) = 0$ when $x \leqslant 0$ and $\mathrm{h}(x) = 1$ when $x > 0$; and $\langle \mathrm{d}p\rangle$ represents the Macaulay bracket, given that $\langle \mathrm{d}p\rangle = \mathrm{d}p$ when $\mathrm{d}p > 0$ and when $\mathrm{d}p < 0$.

The elastic bulk and shear moduli are given by

$$K_e = \frac{1+e}{\kappa} p_a \left(\frac{p}{p_a}\right)^{0.5} \tag{16}$$

where κ is the material parameter associated with the isotropic compression unloading, given by $\kappa = \kappa_0[(1+e)/(2.97-e)]^2$ in which κ_0 is the material parameter.

The plastic bulk modulus is defined as [50]

$$K_p = \frac{1+e}{\lambda - \kappa} p_a \left(\frac{p}{p_a}\right)^{0.5} \frac{M_c g(\theta)}{M_c g(\theta) - R} \tag{17}$$

where λ is the material parameter associated with the isotropic compression loading, given by $\lambda = \lambda_0[(1+e)/(2.97-e)]^2$ in which λ_0 is the material parameter.

The macro volumetric strain induced by dilatancy involves a set of micro volumetric strains caused by dilatancy in the micro shear structures, given by

$$\mathrm{d}\varepsilon_{vd} = \sum_{n=1}^{N}\sum_{k=1}^{3} 2w^{(n)}\mathrm{d}\varepsilon_{vd}^{(nk)} \tag{18}$$

where $\varepsilon_{vd}^{(nk)}$ represents the kth micro volumetric strain component caused by dilatancy in the nth micro shear structure. According to the experimental results of cyclic torsional shear tests [51], the microscopic stress–dilatancy relation is defined as

$$\mathrm{d}\varepsilon_{vd}^{(nk)} = d_1(\pm r_d^{(nk)} - r^{(nk)})\mathrm{d}\gamma_p^{(nk)} \tag{19}$$

where d_1 represents the micro dilatancy constant, assuming that the micro dilatancy constant is the same for all micro shear structures; $\gamma_p^{(nk)}$ refers to the micro plastic shear strain, defined in Eq. (A9) in the Appendix A; and $\pm$ is taken as positive when $\mathrm{d}\gamma_p^{(nk)} > 0$ and negative when $\mathrm{d}\gamma_p^{(nk)} < 0$.

2.6. Micro shear deformation

Following the theory of bounding surface plasticity [50], the incremental stress–strain relationship for the micro shear deformation can be written as (see A.2 in the Appendix A for the derivation procedures)

$$\mathrm{d}\gamma^{(nk)} = \frac{1}{G_e^{(nk)}}\mathrm{d}\tau^{(nk)} + \frac{1}{G_p^{(nk)}} p\mathrm{d}r^{(nk)} + \frac{1}{H_p^{(nk)}}\mathrm{h}(p - p_m)\frac{\langle \mathrm{d}p\rangle}{|\mathrm{d}p|} r^{(nk)}\mathrm{d}p \tag{20}$$

where $\gamma^{(nk)}$ represents the micro shear strain; $G_e^{(nk)}$ refers to the micro elastic modulus, which can be calculated by the macro elastic shear modulus (see A.5 in the Appendix A); and $G_p^{(nk)}$ and $H_p^{(nk)}$ denote the micro plastic shear moduli associated with $\mathrm{d}r^{(nk)}$ and $\mathrm{d}p$, respectively.

Based on the multishear bounding surface model for isotropic sands [44], the micro plastic shear modulus $G_p^{(nk)}$ related to $\mathrm{d}r^{(nk)}$ is defined as

$$G_p^{(nk)} = h_1 \exp(h_2(A-1)) G_e^{(nk)} \left(\frac{r_b^{(nk)}}{r_m^{(nk)}}\frac{\bar{\rho}_1^{(nk)}}{\rho_1^{(nk)}} - 1\right) \tag{21}$$

where h_1 and h_2 denote model constants; $\rho_1^{(nk)} = |r^{(nk)} - r_r^{(nk)}|$ represents the distance between the current point and the projection center for the micro stress ratio; $r_r^{(nk)}$ refers to the projection center of the micro stress ratio, defined as the last inflection point of the micro stress ratio in the reverse loading or the origin in the virgin loading; and $\bar{\rho}_1^{(nk)} = |\pm r_m^{(nk)} - r_r^{(nk)}|$ represents the distance between the maximum point and the projection center for the micro stress ratio, in which $\pm$ is taken as positive when $\mathrm{d}r^{(nk)} > 0$ and negative when $\mathrm{d}r^{(nk)} < 0$. Note

Table 1
Model constants for Toyoura sand.

Elasticity	Critical state	Plastic modulus	Dilatancy	Fabric
$G_0 = 125$	$M_c = 1.25$	$h_1 = 0.7$	$d_1 = 0.4$	$F_{d0} = 0.45$
$\kappa_0 = 0.01$	$e_\Gamma = 0.934$	$h_2 = 1.8$	$n_d = 7.0$	$k_1 = 0.016$
	$\lambda_c = 0.019$	$h_3 = 0.5$		$k_2 = 8.03$
	$n_c = 0.7$	$n_b = 3.0$		$e_A = 0.11$
		$\lambda_0 = 0.02$		

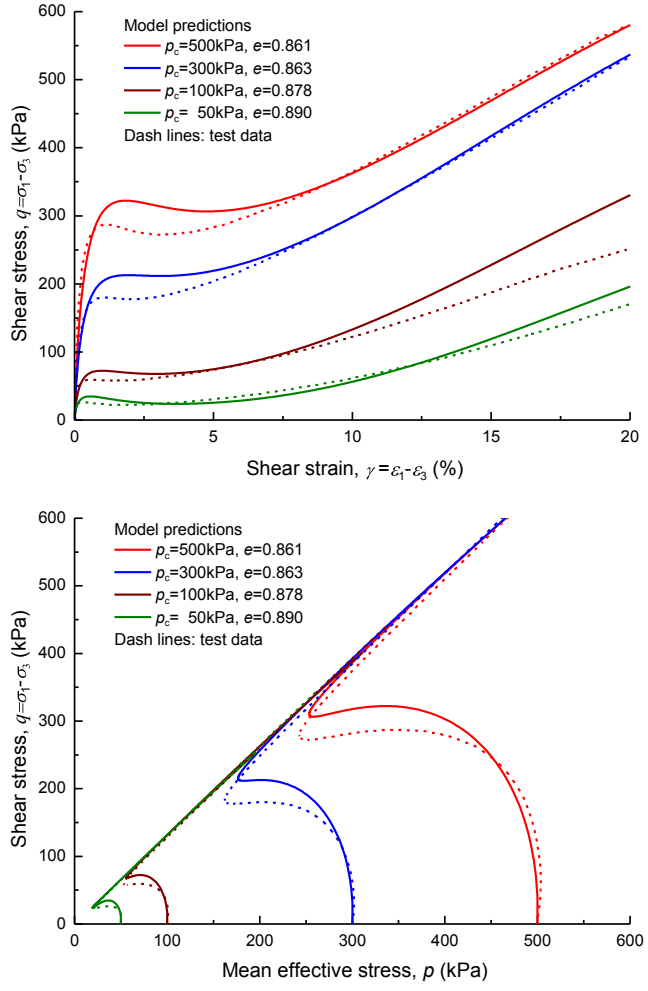

Fig. 5. Test and simulation results on undrained triaxial compression tests.

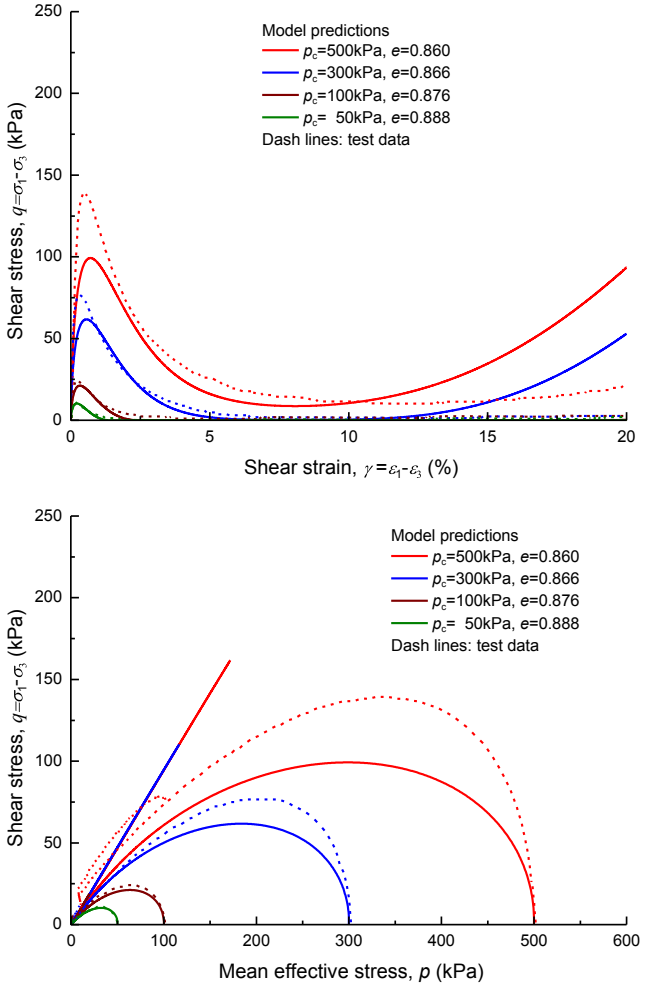

Fig. 6. Test and simulation results on undrained triaxial extension tests.

that the introduction of the term with the scalar variable of fabric anisotropy A in Eq. (21) better simulates the constitutive response of sands.

The micro plastic shear modulus $H_p^{(nk)}$ related to dp is given by [44]

$$H_p^{(nk)} = h_3 G_e^{(nk)} \frac{r_c^{(nk)}}{r^{(nk)}} \frac{\bar{\rho}_2}{\rho_2} \tag{22}$$

where h_3 refers to the model constant; $\rho_2 = |p - p_r|$ represents the distance between the current point and the projection center for the mean effective stress; p_r denotes the projection center of the mean effective stress, defined as the last inflection point of the mean effective stress in the reverse loading or the origin in the virgin loading; and $\bar{\rho}_2 = |p_m - p_r|$ refers to the distance between the maximum point and the projection center for the mean effective stress, in which $\bar{\rho}_2 = p_r$ when dp < 0.

2.7. Macro stress–strain relationship

The incremental relationship between the macro stress and strain can be expressed as

$$d\sigma_{ij} = D_{ijst} d\varepsilon_{st} \tag{23}$$

where D_{ijst} represents the macro elastoplastic stiffness tensor associated with the macro and micro quantities (see A.3 in the Appendix A).

3. Model verification

3.1. Calibration of model constants

The proposed model has 17 constants: two constants related to the elasticity (G_0 and κ_0), four constants associated with the critical state (M_c, e_Γ, λ_c, and n_c), five constants related to the plastic modulus (h_1, h_2, h_3, n_b, and λ_0), two constants associated with the dilatancy (d_1 and n_d), and four constants related to the fabric and its evolution (F_{d0}, k_1, k_2, and e_A). These model constants can be calibrated by the following procedures:

(1) G_0 can be determined by the deviator stress versus axial strain relationship at a very small strain of the triaxial compression tests. λ_0 and κ_0 can be inferred according to the e-p relation in the constant stress ratio loading and un-loading in the isotropic consolidation tests, respectively. Alternatively, κ_0 can be obtained from G_0 and the elastic Poisson's ratio by using the linear elasticity relation of the shear and bulk moduli, i.e. $\kappa_0 = 3(1 - 2\nu)/[2(1 + \nu)G_0]$ in which ν is the elastic Poisson's ratio. λ_0 can be set to about 2–10 times of κ_0 if the related test data are not available.
(2) M_c, e_Γ, λ_c, and n_c can be obtained directly from the results of the triaxial compression tests for the critical state stress ratio and the critical state line in the e-p plane.
(3) F_{d0} depends on the particle characteristics and sample preparation methods. Its quantification is a continuing research challenge. It can be estimated by small strain measurements performed in

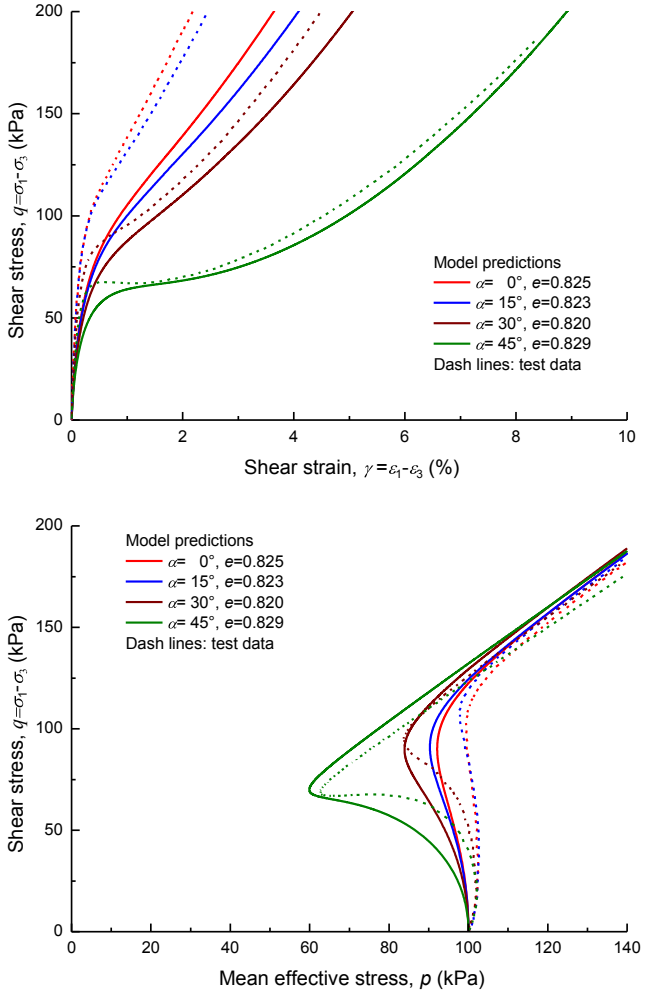

Fig. 7. Test and simulation results on undrained torsional shear tests (p_c = 100 kPa, b = 0).

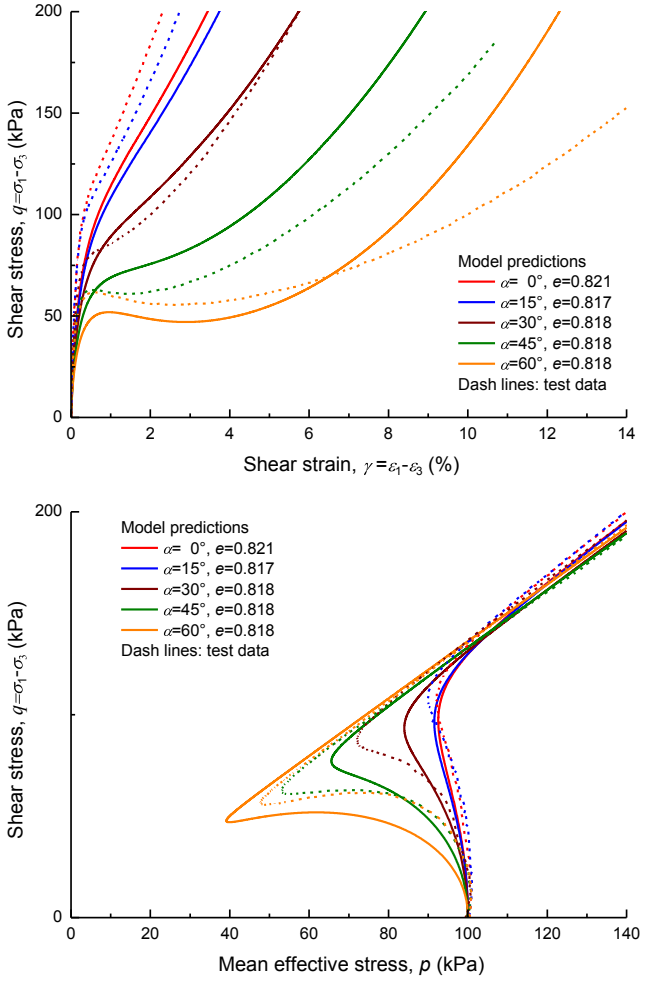

Fig. 8. Test and simulation results on undrained torsional shear tests (p_c = 100 kPa, b = 0.25).

different directions (e.g. bender elements in the horizontal and vertical directions) or by measuring the direction of the sand particles, the spatial distribution of voids, and the anisotropic shear stiffness [7]. Alternatively, it can be determined based on the value of dq/dp at the very beginning of the undrained triaxial tests [33].

(4) By ignoring the small elastic deformation, n_d, e_A, and k_F can be approximately estimated by $M_d = M_c \exp(n_d \zeta)$ and Eqs. (5)–(9) at the phase transformation state, measured from the results of the drained or undrained triaxial compression tests for the three loading cases under different initial states, in which M_d takes the value of the stress ratio at the phase transformation state. Further fitting theses values of k_F into $k_F = k_1 \exp(k_2 e)$ yields k_1 and k_2. After e_A, k_1, and k_2 are determined, n_b can be obtained by $M_b = M_c \exp(-n_b \zeta)$ at the peak stress ratio state, measured from the results of the drained triaxial compression tests, in which M_b takes the value of the stress ratio at the peak stress ratio state. If different test data give different values for these model constants, their average values can be taken. Alternatively, n_b can be estimated by the trial-and-error method if the drained triaxial compression test data are not available.

(5) d_1 can be determined based on stress–dilatancy data such as the relationship between the volumetric and deviatoric strains in the drained triaxial compression tests. Alternatively, it can be obtained by the trial-and-error method if the proper stress–dilatancy data are not available.

(6) h_1, h_2, and h_3 control the value of the plastic modulus and can be determined through the trial-and-error method by best matching the model predictions to the stress–strain curve and the effective stress path in the tests.

3.2. Model performance

Simulations of the laboratory tests by Yoshimine et al. [1] are performed to confirm the prediction ability of the proposed model. The test samples of Toyoura sands were prepared by a dry-deposited method. Yoshimine et al. [1] systematically studied the undrained anisotropic response of sands with a variety of confining pressures and densities under different loading modes and directions through the triaxial compression and extension tests, the hollow cylindrical torsion shear tests, and the simple shear tests. Fig. 4 shows the setup of a hollow cylindrical torsion shear test, in which σ_1, σ_2, and σ_3 represent the major, intermediate, and minor principal stresses, respectively. The intermediate principal stress is fixed in the horizontal direction and its value is equal to the radial normal stress. The major and minor principal stresses are located on the $z-\theta$ plane. The angle α represents the inclining angle of the major principal stress relative to the vertical axis. As shown in Fig. 4, because the deposition plane of the samples is horizontal, this angle also reflects the inclination relationship between the major principal stress and the deposition plane. Torsional shear tests involve the full range of 0°–90° for angle α and 0–1 for the intermediate principal stress ratio b where $b = (\sigma_2 - \sigma_3)/(\sigma_1 - \sigma_3)$. The model constants used in all simulations are listed in Table 1, where the parameters G_0, κ_0, M_c, e_Γ, λ_c, n_c, n_b, d_1, n_d, F_{d0}, and e_A are calibrated with reference

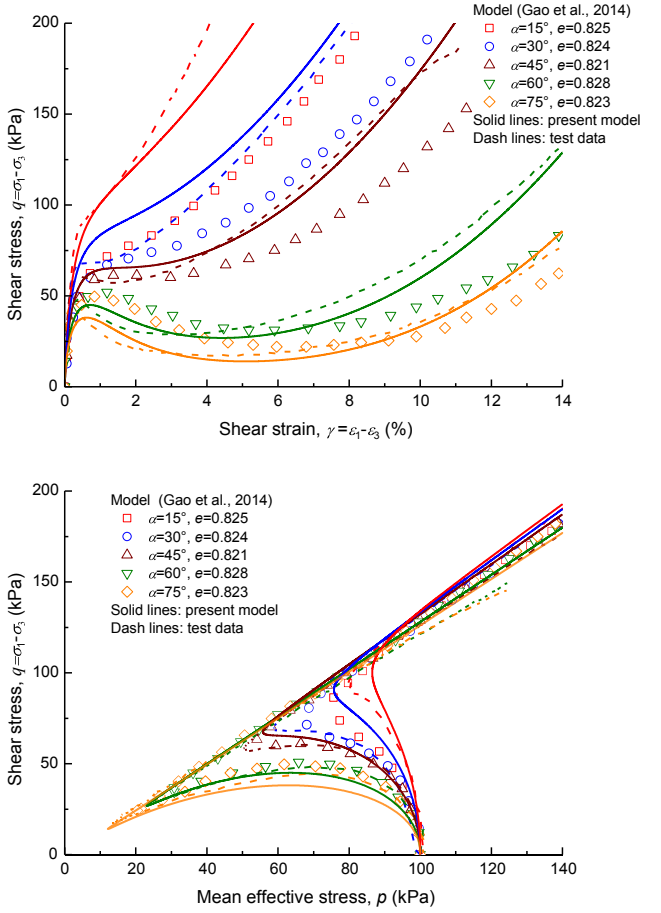

Fig. 9. Test and simulation results on undrained torsional shear tests (p_c = 100 kPa, b = 0.5).

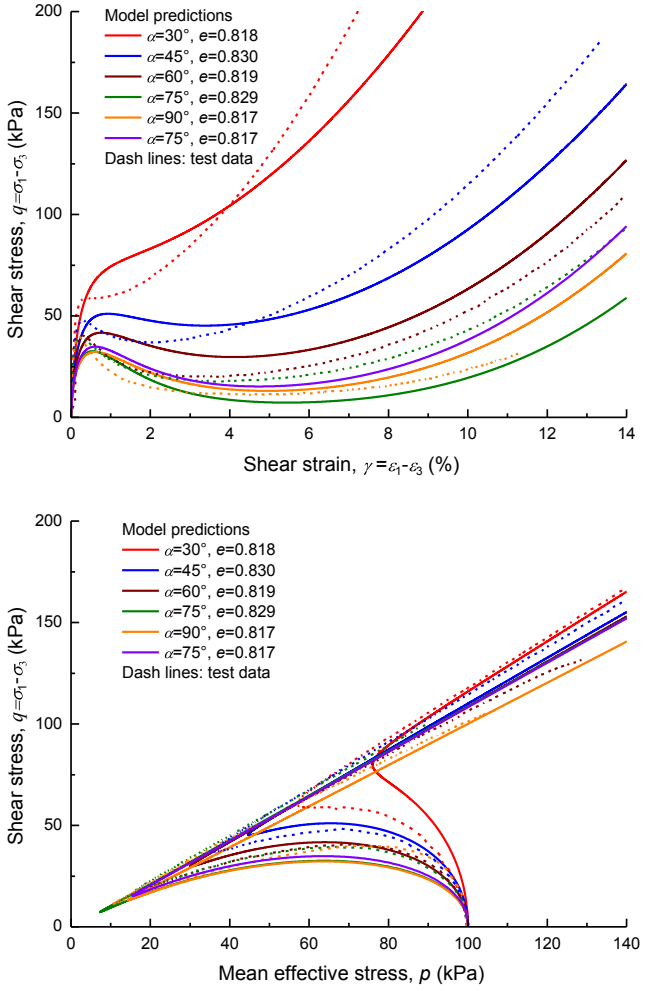

Fig. 10. Test and simulation results on undrained torsional shear tests (p_c = 100 kPa, b = 0.75).

to other macro constitutive models by Li and Dafalias [27] and Gao et al. [32] and λ_0 is set to 2 times of κ_0. Note that some parameter symbols in the proposed model are different from those in the macro constitutive models. In addition, the Matsuoka–Nakai yield criterion is employed in all simulations.

Fig. 5 shows comparisons of the simulation results and experimental data on undrained triaxial compression tests under different initial confining pressures and densities, where p_c is the initial consolidation stress. As can be seen from this figure, the calculated stress–strain curves and effective stress paths are generally consistent with those of the experimental data. The stress–strain curves for p_c = 300 kPa and p_c = 500 kPa agree well with the experimental data except that the peak stresses at low shear strains are overestimated in the calculations. However, there are some differences between the predicted and experimental results at large strains for the stress–strain curves with p_c = 50 kPa and p_c = 100 kPa. Fig. 6 illustrates comparisons of the simulation results and experimental data on undrained triaxial extension tests under different initial confining pressures and densities. As can be observed from this figure, the calculated stress–strain curves and effective stress paths are in good agreement with the experimental data for the cases with p_c = 50 kPa and p_c = 100 kPa. However, for the cases with p_c = 300 kPa and p_c = 500 kPa, the model underestimates the peak shear strengths at low strains and overestimates the dilative responses at relatively large strains after the descending post-peak regime. The above comparisons indicate that the model can reflect the influences of confining pressure and density on sand responses under undrained triaxial compression and extension. Depending on the combination of confining pressure and density associated with the value of the anisotropic state parameter, the simulation results generally exhibit the same characteristics for the dilative and contractive responses as those observed in the tests. Moreover, by comparing Fig. 5 with Fig. 6, it is found that the shear responses for triaxial compression and extension are very different under the same initial confining pressure and density. This different behavior clearly indicates that the initial inherent anisotropy can significantly affect the undrained response of sands.

Figs. 7–11 show comparisons of the simulation results and experimental data for the undrained torsional shear tests under constant values of b = 0, 0.25, 0.5, 0.75, and 1, respectively. Each of the figures describes the experimental and predicted results in the stress–strain relation and the stress path at the same b-value and different inclining angles of the major principal stress relative to the vertical axis. Fig. 7 shows comparisons of the simulation results and experimental data under a constant value of b = 0 and angles of 0°, 15°, 30°, and 45°. As can be seen from Fig. 7, the simulation and test results are close to each other when the angle is equal to 30° and 45°, and there are some differences between them when the angle is equal to 0° and 15°. Fig. 8 shows comparisons of the simulation results and experimental data under a constant value of b = 0.25 and angles of 0°, 15°, 30°, 45°, and 60°. As can be observed from Fig. 8, the model predictions are in good agreement with the test data when the angle is equal to 30°, and there are some differences between them when the angle is equal to other values. In particular, for the cases of 45° and 60°, the calculated stresses are much higher than those of the experimental data because the model overestimates the dilative responses. Fig. 9 shows comparisons of the

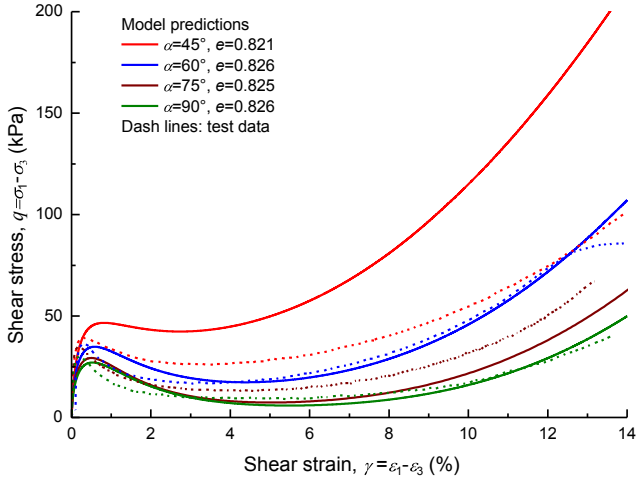

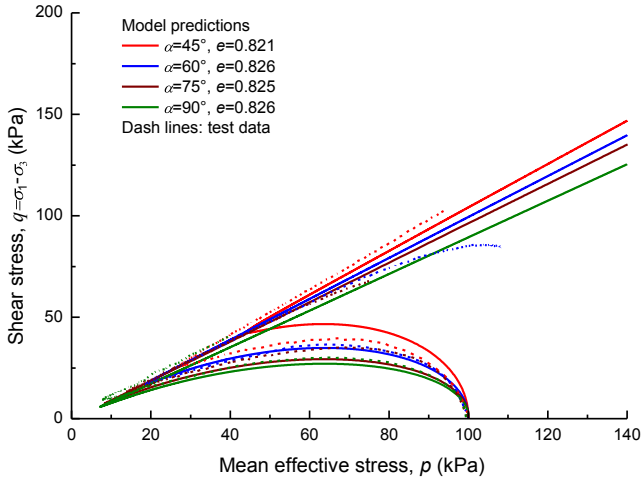

Fig. 11. Test and simulation results on undrained torsional shear tests (p_c = 100 kPa, b = 1).

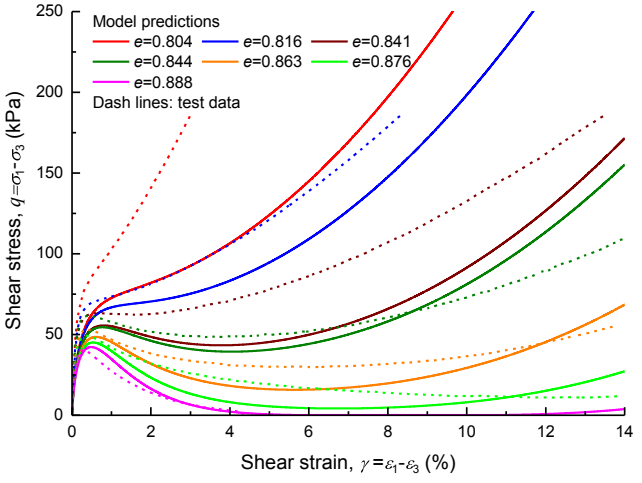

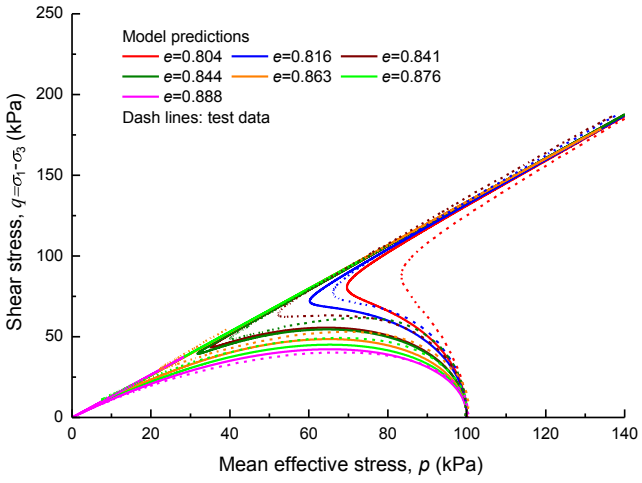

Fig. 12. Test and simulation results on undrained simple shear tests (p_c = 100 kPa, K_0 = 1).

simulation results and experimental data under a constant value of b = 0.5 and angles of 15°, 30°, 45°, 60°, and 75°. As can be seen from Fig. 9, the simulation results are very consistent with the test data for all angles. To compare with the existing macro constitutive models with a similar concept, the simulation result of the macro bounding surface model created by Gao et al. [32] is also illustrated in Fig. 9. A comparison of the simulated results by Gao et al.'s model, the present model, and the experimental data indicates that the present model provides a better prediction than the macro constitutive model in this case. Fig. 10 shows comparisons of the simulation results and experimental data under a constant value of b = 0.75 and angles of 30°, 45°, 60°, 75°, and 90°. As can be observed from Fig. 10, the model predictions are close to the test data when the angle is equal to 30°, 45°, 60°, and 90°, and there are some differences between them when the angle is equal to 75°. Note that the predicted stress–strain curve for the angle of 75° is situated below the curve for the angle of 90°. The reason is that different void ratios are used in the calculations. For convenience of explanation, the result with the same void ratio is shown in violet in Fig. 10, indicating that there is no such reversal. Fig. 11 shows comparisons of the simulation results and experimental data under a constant value of b = 1 and angles of 45°, 60°, 75°, and 90°. As can be seen from Fig. 11, the results of the simulations and tests are in good agreement when the angle is equal to 60° and 90°, and there are some differences between them when the angle is equal to 45° and 75°. Moreover, it can be observed from Figs. 7–11 that the proposed model can accurately predict the overall trends of the sand responses observed in the tests, i.e. the dilative and contractive responses of sands generally increase with an increase in angle α. This characteristic indicates that the fabric anisotropy acts a significant part in the undrained sand response under the same loading in different directions.

Fig. 12 shows comparisons of the simulation results and experimental data from the undrained simple shear tests under initial isotropic consolidation stresses of 100 kPa. K_0 in the figures represents the initial consolidation stress ratio, defined as the initial value of the ratio of the lateral effective stress to the vertical effective stress. Fig. 13 shows comparisons of the simulation results and experimental data for the undrained simple shear tests in the initial anisotropic consolidation state, where the initial vertical effective stress is equal to 200 kPa and K_0 is equal to 0.5. The simulation results in Figs. 12 and 13 show that the model can reasonably predict the general responses of sands observed in undrained simple shear tests under the initial isotropic and anisotropic consolidation states, although there are some differences in magnitude between them.

By comparing the simulated results with the experimental data in Figs. 5–13, it can be concluded that all 41 simulations are able to capture the general trends of the experimental data with a single set of model parameters given in Table 1. These simulation results confirm that the scalar fabric anisotropy variable A and the anisotropic state parameter ζ are very useful in accounting for the effect of fabric anisotropy on the sand responses. As can be seen from the above simulation results, however, in some cases, the simulation results and experimental data are different in magnitude to a certain degree. In fact,

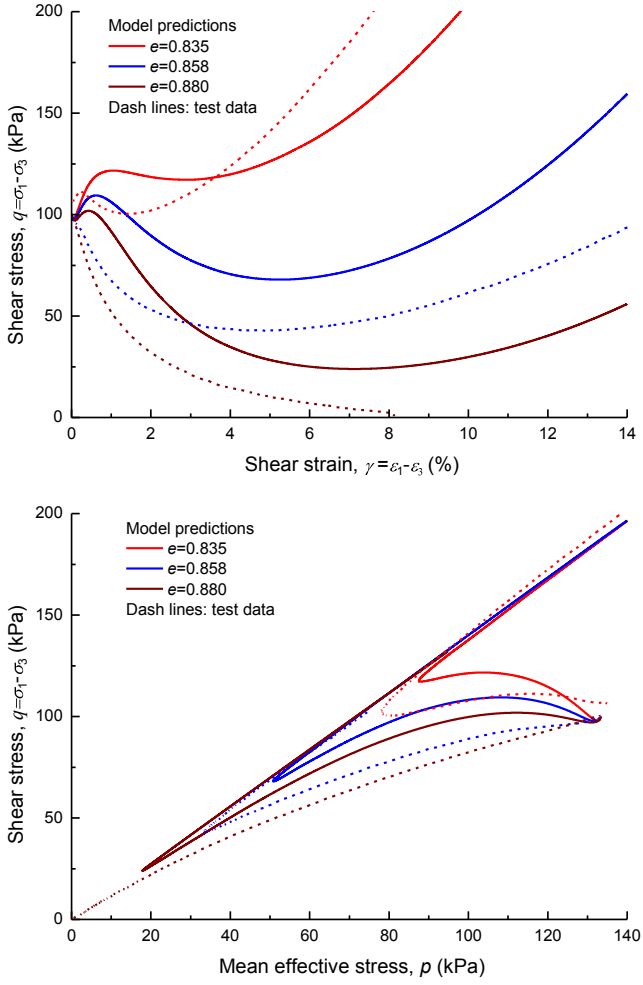

Fig. 13. Test and simulation results on undrained simple shear tests (p_c = 133 kPa, K_0 = 0.5).

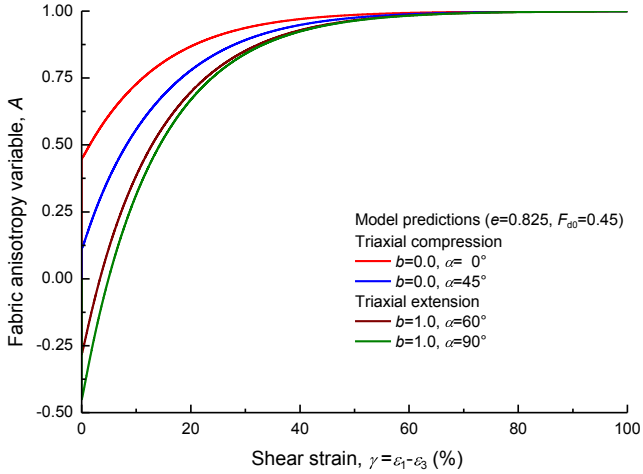

Fig. 14. Evolution of fabric anisotropy variable for triaxial compression and extension.

the parameter e_A, which controls the plastic response of sands, is set as a constant for simplicity in the proposed model, but the dependences of e_A on the confining pressure and density are neglected. By introducing e_A dependent on e and p, the simulated results may be further improved. Therefore, it is necessary to propose a better expression for e_A related to e and p in the future.

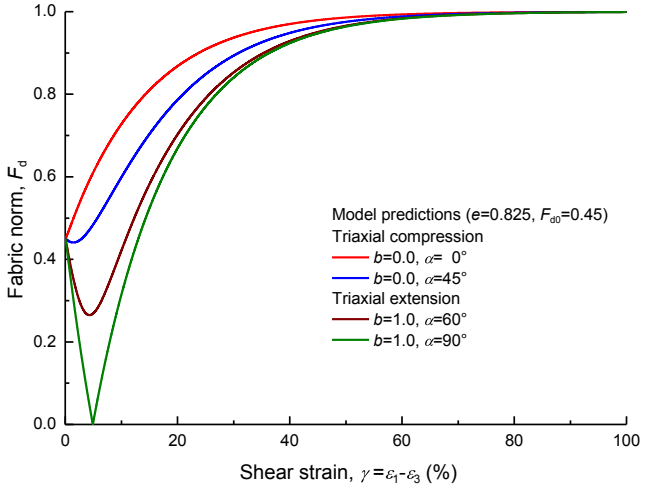

Fig. 15. Evolution of fabric norm for triaxial compression and extension.

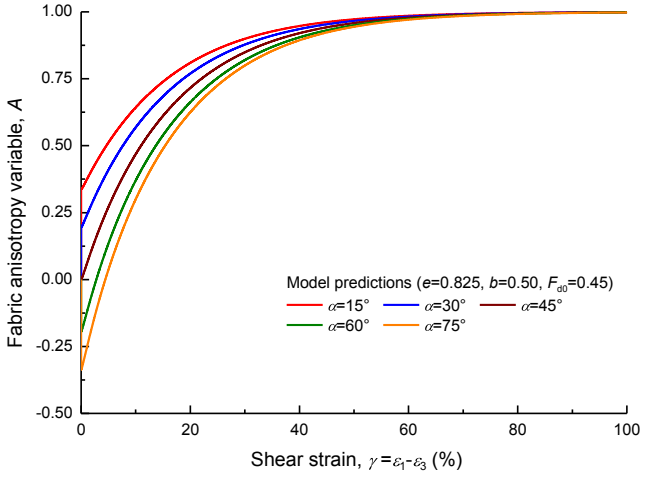

Fig. 16. Evolution of fabric anisotropy variable for torsional shearing.

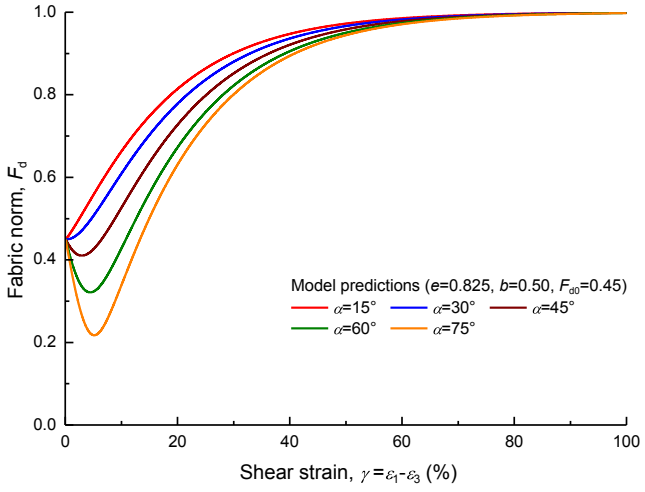

Fig. 17. Evolution of fabric norm for torsional shearing.

3.3. Fabric evolution

Figs. 14 and 15 show the variations of the fabric anisotropy variable and fabric norm with shear strain under triaxial compression (b = 0, α = 0° and b = 0, α = 45°) and extension (b = 1, α = 60° and b = 1,

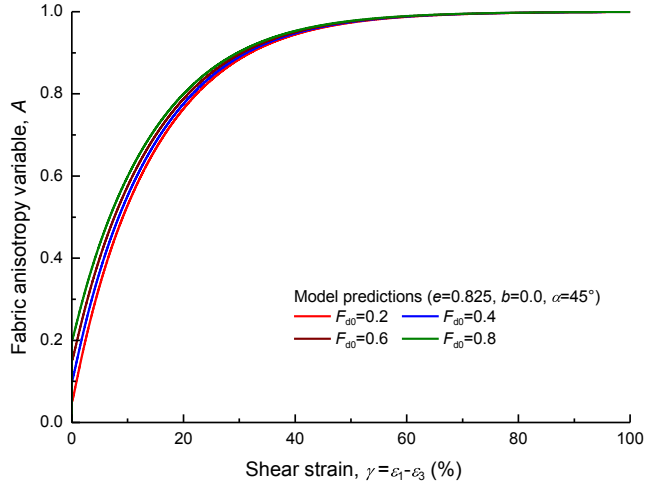

Fig. 18. Evolution of fabric anisotropy variable for different initial degrees of anisotropy.

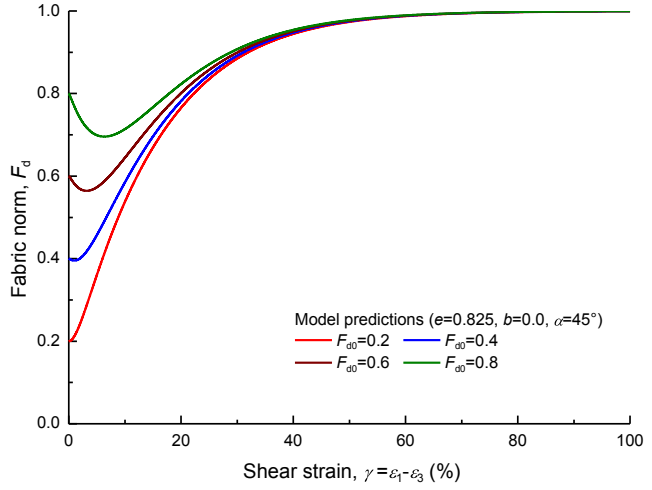

Fig. 19. Evolution of fabric norm for different initial degrees of anisotropy.

$\alpha = 90^{\circ}$), respectively. From these two figures, it can be seen that the fabric anisotropy variable and the fabric norm are directly proportional to the shear strain except that the values of the fabric norm under triaxial extension first decrease and then continuously rise to the critical value of 1. This property is similar to that predicted by the macro constitutive model [27].

Fig. 16 shows the variation of the fabric anisotropy variable with the shear strain for different angles at $b = 0.5$. As can be seen from this figure, the fabric anisotropy variable is directly proportional to the shear strain during loading and finally arrives at the critical value of 1. Fig. 17 illustrates the variation of the fabric norm with shear strain for different angles at $b = 0.5$. As can be observed from the figure, the fabric norm decreases during the initial stage of loading when the angle α is greater than 45°, and then increases to the critical value of 1. The reason for this behavior is that the fabric tensor changes from its initial structure caused by the specimen preparation to that corresponding to the applied stress at $b = 0.5$, while its fabric norm decreases to adapt for this change. However, for a small angle, this adjustment is not very large or there is no such adjustment. The similar behavior in which the fabric norm first decreases and then increases toward its critical state was also confirmed by the results of the DEM simulation [8] and the macro constitutive model [32]. Figs. 16 and 17 also indicate that sands can reach their critical states only at very high strain levels, where the sand fabric is fully adapted to the loading direction, forming a stable anisotropic structure.

Figs. 18 and 19 illustrate the variations of the fabric anisotropy variable and fabric norm with a shear strain under triaxial compression ($b = 0$, $\alpha = 45^{\circ}$) for different initial degrees of anisotropy, respectively. The initial values of the fabric norm used in the simulations are equal to 0.2, 0.4, 0.6, and 0.8. From these two figures, it can be seen that under different initial anisotropies, the fabric anisotropy variables change similarly, while the fabric norms show different characteristics. When the initial fabric norm is greater than 0.4, the fabric norm decreases in the initial loading stage and then increases to a critical value of 1. In addition, the fabric anisotropy variable varies little with the initial anisotropy, while the fabric norm varies greatly.

4. Conclusions

This paper presented a multishear bounding surface model for anisotropic sands in the framework of the bounding surface plasticity theory and anisotropic critical state theory. This originated from an existing multishear model for isotropic sands. The main features and conclusions of the model can be summarized as follows:

(1) The model describes the complex multiaxial behavior of sands by superposing a one-dimensional macro volumetric response and a set of spatially distributed one-dimensional virtual micro shear responses. With this simple decomposition approach, the model can automatically account for the noncoaxial behavior of strain and stress increments without requiring additional model parameters, while most macroscopic constitutive models lack this capability.
(2) The model adopts a simple evolution law of the fabric tensor dependent on the deviatoric plastic strain and considers the effect of evolving fabric anisotropy on sand responses. Following this evolution law, the sand fabric evolves toward the loading direction with the development of the deviatoric plastic strain, and finally reaches the critical structure.
(3) The model uses the anisotropic state parameter in the expressions of the plastic modulus and dilatancy. Thus, the model satisfies the anisotropic critical state theory and has a unique critical state line and unique critical fabric at the critical state.
(4) The model was used to simulate a series of undrained laboratory tests on saturated Toyoura sand specimens prepared by the dry-deposited approach under different confining pressures, densities, principal stress directions, and intermediate principal stress ratios. A comparison between the experimental data and model predictions indicated that the model captured the complex behavior of sands with a single set of model parameters.

Acknowledgements

The authors would like to thank the reviewers for their creative suggestions and expert comments. The authors also would like to thank Professor M. Yoshimine of Tokyo Metropolitan University for sharing his test results and Professor Z. X. Yang of Zhejiang University for his suggestions in this work, and acknowledge the financial supports from the National Natural Science Foundation of China (No. 51878605) as well as the Zhejiang Provincial Natural Science Foundation of China (No. LY16D020002).

Appendix A. . Constitutive relation

A.1. Stress–strain relationship for macro volumetric deformation

The volumetric strain increment includes elastic and plastic parts, i.e.

$$d\varepsilon_v = d\varepsilon_v^e + d\varepsilon_v^p \tag{A1}$$

where ε_v^e and ε_v^p are the elastic and plastic volumetric strains, respectively. Moreover, the plastic volumetric strain involves one caused by a change in the mean effective stress and one caused by dilatancy.

The elastic volumetric strain increment is given by

$$d\varepsilon_v^e = \frac{1}{K_e} dp \tag{A2}$$

The plastic volumetric strain increment without one caused by dilatancy is given by

$$d\varepsilon_v^p - d\varepsilon_{vd} = \frac{1}{K_p} h(p - p_m) \frac{\langle dp \rangle}{|dp|} dp \tag{A3}$$

From Eqs. (A1)–(A3), the incremental relationship between the mean effective stress and volumetric strain can be expressed as

$$d\varepsilon_v - d\varepsilon_{vd} = \frac{1}{K_e} dp + \frac{1}{K_p} h(p - p_m) \frac{\langle dp \rangle}{|dp|} dp \tag{A4}$$

Eq. (A4) can also be written as

$$d\varepsilon_v - d\varepsilon_{vd} = \frac{1}{K} dp \tag{A5}$$

where K is the bulk modulus, given by

$$K = \left(\frac{1}{K_e} + \frac{1}{K_p} h(p - p_m) \frac{\langle dp \rangle}{|dp|} \right)^{-1} \tag{A6}$$

A.2. Stress–strain relationship for micro shear deformation

The micro shear strain increment includes elastic and plastic parts, i.e.

$$d\gamma^{(nk)} = d\gamma_e^{(nk)} + d\gamma_p^{(nk)} \tag{A7}$$

where $\gamma_e^{(nk)}$ is the micro elastic shear strain. Its increment is given by

$$d\gamma_e^{(nk)} = \frac{1}{G_e^{(nk)}} d\tau^{(nk)} \tag{A8}$$

The micro plastic shear strain increment is given by

$$d\gamma_p^{(nk)} = \frac{1}{G_p^{(nk)}} p dr^{(nk)} + \frac{1}{H_p^{(nk)}} h(p - p_m) \frac{\langle dp \rangle}{|dp|} r^{(nk)} dp \tag{A9}$$

From Eqs. (A7)–(A9), the micro shear strain increment can be expressed as

$$d\gamma^{(nk)} = \frac{1}{G_e^{(nk)}} d\tau^{(nk)} + \frac{1}{G_p^{(nk)}} p dr^{(nk)} + \frac{1}{H_p^{(nk)}} h(p - p_m) \frac{\langle dp \rangle}{|dp|} r^{(nk)} dp \tag{A10}$$

A.3. Macro stress–strain relationship

The micro shear stress increment can be written as

$$d\tau^{(nk)} = p dr^{(nk)} + r^{(nk)} dp \tag{A11}$$

From Eqs. (A10) and (A11), the micro shear stress increment can be expressed by

$$d\tau^{(nk)} = G^{(nk)} d\gamma^{(nk)} + (1 - G^{(nk)}/H^{(nk)}) r^{(nk)} dp \tag{A12}$$

where $G^{(nk)}$ and $H^{(nk)}$ are micro shear moduli related to the micro stress ratio and mean effective stress, respectively, given by

$$G^{(nk)} = \left(\frac{1}{G_e^{(nk)}} + \frac{1}{G_p^{(nk)}} \right)^{-1} \tag{A13}$$

$$H^{(nk)} = \left(\frac{1}{G_e^{(nk)}} + \frac{1}{H_p^{(nk)}} h(p - p_m) \frac{\langle dp \rangle}{|dp|} \right)^{-1} \tag{A14}$$

From Eqs. (18), (19), (A7), (A8), and (A12), the volumetric strain increment caused by dilatancy can be expressed by

$$d\varepsilon_{vd} = \sum_{n=1}^{N}\sum_{k=1}^{3} 2w^{(n)} d_1(\pm r_d^{(nk)} - r^{(nk)})\{(1 - \frac{G^{(nk)}}{G_e^{(nk)}})d\gamma^{(nk)} - \frac{1}{G_e^{(nk)}}(1 - \frac{G^{(nk)}}{H^{(nk)}})r^{(nk)}dp\} \tag{A15}$$

Substituting Eq. (A15) into Eq. (A5) yields

$$dp = K_1\{d\varepsilon_v - \sum_{n=1}^{N}\sum_{k=1}^{3} 2w^{(n)} d_1(\pm r_d^{(nk)} - r^{(nk)})(1 - G^{(nk)}/G_e^{(nk)})d\gamma^{(nk)}\} \tag{A16}$$

where K_1 is given by

$$K_1 = \frac{K}{1 - K\sum_{n=1}^{N}\sum_{k=1}^{3} 2w^{(n)} d_1(\pm r_d^{(nk)} - r^{(nk)})r^{(nk)}(1 - G^{(nk)}/H^{(nk)})/G_e^{(nk)}} \tag{A17}$$

From Eqs. (1), (3), (A12), and (A16), the incremental relationship of the macro stress and strain can be expressed as

$$d\sigma_{ij} = D_{ijst}\, d\varepsilon_{st} \tag{A18}$$

where D_{ijst} is given by

$$D_{ijst} = K_1 Q_{ij}\delta_{st} + \sum_{n=1}^{N}\sum_{k=1}^{3} 2w^{(n)}(-Q^{(nk)}Q_{ij} + G^{(nk)}N_{ij}^{(nk)})N_{st}^{(nk)} \tag{A19}$$

where

$$Q_{ij} = \delta_{ij} + \sum_{n=1}^{N}\sum_{k=1}^{3} 2w^{(n)} r^{(nk)}(\,1 - G^{(nk)}/H^{(nk)})N_{ij}^{(nk)} \tag{A20}$$

$$Q^{(nk)} = K_1 d_1(\pm r_d^{(nk)} - r^{(nk)})(1 - G^{(nk)}/G_e^{(nk)}) \tag{A21}$$

A.4. Relationship between macro and micro stress ratio parameters

The relationship between the micro and macro stress ratio parameters can be expressed as [44]

$$r_i^{(nk)} = \frac{2}{3}\frac{M_i g(\theta)}{\sum_{n=1}^{N}\sum_{k=1}^{3} 2w^{(n)}\ |N_{33}^{(nk)}|}\ (i = \mathrm{b},\ \mathrm{c}, \mathrm{d}) \tag{A22}$$

A.5. Relationship between macro and micro elastic shear moduli

The relationship of the micro and macro elastic shear moduli can be expressed as [44]

$$G_e^{(nk)} = \frac{4}{3}\frac{G_e}{\sum_{n=1}^{N}\sum_{k=1}^{3} 2w^{(n)}\ |N_{33}^{(nk)}|^2} \tag{A23}$$

where G_e is the macro elastic shear modulus, given by the empirical equation [52] as

$$G_e = G_0\frac{(2.97 - e)^2}{1 + e}p_a\left(\frac{p}{p_a}\right)^{0.5} \tag{A24}$$

where G_0 is the elastic shear modulus parameter.

References

[1] Yoshimine M, Ishihara K, Vargas W. Effects of principal stress direction and intermediate principal stress on drained shear behavior of sand. Soils Found 1998;38(3):177–86.
[2] Yang ZX, Li XS, Yang J. Quantifying and modelling fabric anisotropy of granular soils. Géotechnique 2008;58(4):237–48.
[3] Sun D, Huang W, Yao Y. An experimental study of failure and softening in sand under three-dimensional stress condition. Granular Matter 2008;10:187–95.
[4] Sze HY, Yang J. Failure modes of sand in undrained cyclic loading: impact of sample preparation. J Geotech Geoenviron Eng 2014;140(1):152–69.
[5] Yang J, Luo XD. Exploring the relationship between critical state and particle shape for granular materials. J Mech Phys Solids 2015;84:196–213.
[6] Oboudi M, Pietruszczak S, Razaqpur AG. Description of inherent and induced anisotropy in granular media with particles of high sphericity. Int J Geomech 2016. https://doi.org/10.1061/(ASCE)GM.1943-5622.0000635, 04016006.
[7] Fonseca J, O'Sullivan C, Coop MR, Lee PD. Quantifying the evolution of soil fabric during shearing using scalar parameters. Géotechnique 2013;63(10):818–29.
[8] Li X, Li XS. Micro-macro quantification of the internal structure of granular materials. J Eng Mech 2009;135(7):641–56.
[9] Yimsiri S, Soga K. DEM analysis of soil fabric effects on behaviour of sand. Géotechnique 2010;60(6):483–95.
[10] Zhao J, Guo N. Unique critical state characteristics in granular media considering fabric anisotropy. Géotechnique 2013;63(8):695–704.
[11] Yang ZX, Wu Y. Critical state for anisotropic granular materials: a discrete element perspective. Int J Geomech 2016. https://doi.org/10.1061/(ASCE)GM.1943-5622.0000720, 04016054.
[12] Wang R, Fu P, Zhang JM, Dafalias YF. Evolution of various fabric tensors for granular media toward the critical state. J Eng Mech 2017;143(10):04017117.
[13] Li XS, Dafalias YF. Constitutive modeling of inherently anisotropic sand behavior. J Geotech Geoenviron Eng 2002;128(10):868–80.
[14] Li XS, Dafalias YF. A constitutive framework for anistropic sand including non-proportional loading. Géotechnique 2004;54(1):41–55.
[15] Dafalias YF, Papadimitriou AG, Li XS. Sand plasticity model accounting for inherent fabric anisotropy. J Eng Mech 2004;130(11):1319–33.
[16] Yin ZY, Chang CS, Hicher PY. Micromechanical modeling for effect of inherent anisotropy on cyclic behavior of sand. Int J Solids Struct 2010;47(14–15):1933–51.
[17] Schadlich B, Schweiger HF. A multilaminate constitutive model accounting for anisotropic small strain stiffness. Int J Numer Anal Meth Geomech 2013;37(10):1337–62.
[18] Golchin A, Lashkari A. A critical state sand model with elastic-plastic coupling. Int J Solids Struct 2014;51:2807–25.
[19] Tengattini A, Das A, Einav I. A constitutive modelling framework predicting critical state in sand undergoing crushing and dilation. Géotechnique 2016;66(9):695–710.
[20] Tasiopoulou P, Gerolymos N. Constitutive modelling of sand: a progressive calibration procedure accounting for intrinsic and stress-induced anisotropy. Géotechnique 2016;66(9):754–70.
[21] Rahimi M, Chan D, Nouri A, Rasouli R. Effects of inherent fabric anisotropy and intermediate principal stress on constitutive behavior of uncemented and cemented

sands. Comput Geotech 2016;80:237–47.
[22] Dafalias YF, Taiebat M. SANISAND-Z: zero elastic range sand plasticity model. Géotechnique 2016;66:999–1013.
[23] Sadrnejad SA, Shakeri S. Multilaminate non-coaxial modelling of anisotropic sand behavior through damage formulation. Comput Geotech 2017;88:18–31.
[24] Lashkari A, Karimi A, Fakharian K, Kaviani-Hamedani F. Prediction of undrained behavior of isotropically and anisotropically consolidated firoozkuh sand: instability and flow liquefaction. Int J Geomech 2017. https://doi.org/10.1061/(ASCE)GM.1943-5622.0000958, 04017083.
[25] Wan RG, Guo PJ. Stress dilatancy and fabric dependencies on sand behavior. J Eng Mech 2004;130(6):635–45.
[26] Wan RG, Nicot F, Darve F. Micromechanical formulation of stress dilatancy as flow rule in plasticity of granular materials. J Eng Mech 2009;136(5):589–98.
[27] Li XS, Dafalias YF. Anisotropic critical state theory: the role of fabric. J Eng Mech 2012;138(3):263–75.
[28] Been K, Jefferies MG. A state parameter for sands. Géotechnique 1985;35(2):99–112.
[29] Iai S, Tobita T, Ozutsumi O. Induced fabric under cyclic and rotational loads in a strain space multiple mechanism model for granular materials. Int J Numer Anal Meth Geomech 2013;37(2):150–80.
[30] Kruyt NP. Micromechanical study of fabric evolution in quasi-static deformation of granular materials. Int J Solids Struct 2010;44:120–9.
[31] Kruyt NP, Rothenburg L. A micromechanical study of dilatancy of granular materials. J Mech Phys Solids 2016;95:411–27.
[32] Gao Z, Zhao J, Li XS, Dafalias YF. A critical state sand plasticity model accounting for fabric evolution. Int J Numer Anal Meth Geomech 2014;38(4):370–90.
[33] Zhao J, Gao Z. Unified anisotropic elastoplastic model for sand. J Eng Mech 2015;142(1):04015056.
[34] Woo SI, Salgado R. Bounding surface modeling of sand with consideration of fabric and its evolution during monotonic shearing. Int J Solids Struct 2015;63:277–88.
[35] Gao Z, Zhao J. Constitutive modeling of anisotropic sand behavior in monotonic and cyclic loading. J Eng Mech 2015;141(8):04015017.
[36] Gao Z, Zhao J. A non-coaxial critical-state model for sand accounting for fabric anisotropy and fabric evolution. Int J Solids Struct 2017;106–107:200–12.
[37] Yang ZX, Xu TT, Chen YN. Unified mdeling of the influence of consolidation conditions on monotonic soil response considering fabric evolution. J Eng Mech 2018;144(8):04018073.
[38] Dashti H, Sadrnejad SA, Ganjian N. Multi-directional modeling for prediction of fabric anisotropy in sand liquefaction. Comput Geotech 2017;92:156–8.
[39] Wheeler SJ, Näätänen A, Karstunen M, Lojander M. An anisotropic elastoplastic model for soft clays. Can Geotech J 2003;40(2):403–18.
[40] Castro J, Karstunen M. Numerical simulations of stone column installation. Can Geotech J 2010;47(10):1127–38.
[41] Rezania M, Sivasithamparam N, Nezhad MM. On the stress update algorithm of an advanced critical state elasto-plastic model and the effect of yield function equation. Finite Elem Anal Des 2014;90:74–83.
[42] Rezania M, Nezhad MM, Zanganeh H, Castro J, Sivasithamparam N. Modeling pile setup in natural clay deposit considering soil anisotropy, structure, and creep effects: case study. Int J Geomech 2017;17(3):04016075.
[43] Fang HL. A state dependent multimechanism model for sands. Géotechnique 2003;53(4):407–20.
[44] Fang HL, Zheng H, Zheng J. Micromechanics-based multimechanism bounding surface model for sands. Int J Plast 2017;90:242–66.
[45] Taylor GI. The plastic strain of metals. J Inst Metals 1938;62:307–24.
[46] Caner FC, Bažant ZP. Impact comminution of solids due to local kinetic energy of high shear strain rate: II – Microplane model and verification. J Mech Phys Solids 2014;64:236–48.
[47] Oda M. Fabric tensor and its geometrical meaning. In: Oda M, Iwashita K, editors. Introduction to mechanics of granular materials. Rotterdam, The Netherlands: Balkema; 1999. p. 27–35.
[48] Matsuoka H, Nakai T. Stress-deformation and strength characteristics of soil under three different principal stresses. Proc JSCE 1974;232:59–70.
[49] Lade PV, Duncan JM. Elastoplastic stress-strain theory for cohesionless soil. J Geotech Eng 1975;101(10):1037–53.
[50] Wang ZL, Dafalias YF, Shen CK. Bounding surface hypoplasticity model for sand. J Eng Mech 1990;116(5):983–1001.
[51] De Silva IN, Koseki J, Wahyudi S, Sato T. Stress-dilatancy relationships of sand in the simulation of volumetric behaviour during cyclic torsional shear loadings. Soils Found 2014;54(4):845–58.
[52] Richart F, Hall J, Woods R. Vibrations of soils and foundations. International series in theoretical and applied mechanics. Englewood Cliffs, NJ, USA: Prentice-Hall; 1970.